




Research Article

Effects of Ti-precursor concentration and annealing temperature on structural and morphological properties of TiO₂ nano-aerogels synthesized in supercritical ethanol

S. Chelbi¹ · D. Djouadi¹  · A. Chelouche¹ · L. Hammiche¹ · T. Touam^{2,3} · A. Doghmane²

Received: 9 January 2020 / Accepted: 30 March 2020 / Published online: 10 April 2020
© Springer Nature Switzerland AG 2020

Abstract

TiO₂ nano-aerogels are elaborated by using acid-modified sol–gel approach from titanium tetra isopropoxide under supercritical drying conditions of ethanol. The effects of Ti-precursor concentration and annealing temperature on structural and morphological properties of TiO₂ nanoparticles are investigated by XRD, infrared spectroscopy, SEM and specific surface area measurements. It was found, from XRD analysis, that pure anatase phase is obtained for the aerogels synthesized with various precursor concentrations. The increase of sol concentration leads to a slight and uniform variation of TiO₂ cell parameters. The specific surface area of aerogels particles decreases and the pore volume increases with increasing of Ti-concentration. The presence of Ti–O and Ti–O–Ti bonds is confirmed by FTIR measurements. EDAX analysis shows that TiO₂ nano-aerogels are oxygen rich. SEM images put into evidence the almost spherical elaborated particles with an enhanced agglomeration at high precursor concentration. With the increase of annealing temperature, the mixture of the phases did not happen and the pure anatase to pure rutile transition phase temperature is found to be around 900 °C. The Ti–O–C bonds disappear with annealing temperature. The heat treatment leads not only to the changes in crystal structure but also in morphology of the elaborated aerogels grains.

Keywords TiO₂ nano-aerogels · Supercritical ethanol · Annealing · Ti-precursor concentration · Structure · Morphology

1 Introduction

Nowadays, a great deal of research interest is shown all over the world in the investigation of Titanium dioxide (TiO₂) which is one of the most attractive materials in nanoscience and nanotechnology for its very important photocatalytic properties [1], high catalytic activity [2, 3], chemical stability [4], low cost and non-toxicity [5]. TiO₂ crystallites are known to be chemically very stable and strongly active to degrade organic compounds. The most promising application of photocatalysis under UV–Vis radiation has largely been studied [6, 7]. Moreover, it should

be noted that TiO₂ can be used in several practical applications, such as: catalysis of photo-degradation of pollutants [8, 9], alcohol dehydration reaction [10], oxidation of aromatic compounds and nitrogen oxide reduction [11]. Titanium dioxide exists in three allotropic forms: anatase, rutile and brookite [12].

However, several studies have shown that photocatalytic activity of titania is greatly affected by several parameters, in particular, crystalline phase [13, 14], crystallites size [15], specific surface area [16] and preparation techniques [17]. In fact, not only different results are obtained for each synthesis methods, but even for the

✉ D. Djouadi, djameldjouadi@yahoo.fr | ¹Laboratoire de Génie de l'Environnement, Université de Bejaia, 06000 Bejaia, Algeria. ²Laboratoire des Semi-Conducteurs, Département de Physique, Faculté des Sciences, Université Badji Mokhtar-Annaba, 23000 Annaba, Algeria. ³Unité de Recherche en Optique et Photonique Centre de Développement des Technologies Avancées, Université de Sétif, 1 Campus El-Bez, 19000 Sétif, Algeria.



same method, size and morphology of the particles are found to be dependent on the concentration of reagents and others experimental parameters [18]. Several methods have been used to synthesis of TiO_2 nanostructures including continuous reaction [19], thermal precipitation [20], chemical phase decomposition vapor [21], solvothermal crystallization [22], ultrasonic irradiation [23] and sol-gel [24]. However, experimental parameters strongly affect structural and morphological properties of particles. These methods lead, in general, to a mixture of crystal phases of titania when annealing temperature is increased. Fortunately, the sol-gel process is considered one of the best elaboration approaches for the preparation of ultrafine titanium dioxide nanoparticles [17]. The sol-gel process followed by drying in supercritical conditions of alcohols is one of the most promising pathways to synthesis nanostructured aerogels of different metal oxides because it controls the size, shape, size distribution and crystalline phase of nanocrystallites.

In this context, we successfully prepared titanium dioxide aerogels by sol-gel process associated with drying at supercritical conditions of ethanol using titanium tetra-isopropoxide (TTIP) as precursor. Then, structural and morphological properties of the elaborated aerogels are investigated. Finally, the effects of Ti-precursor concentration and the annealing temperature on the structural and morphological characteristics of the TiO_2 nanostructured aerogels are discussed.

2 Materials and methods

Pure TiO_2 aerogels were synthesized with different precursor concentrations through the addition of various volumes of titanium tetra-isopropoxide (TTIP) [$\text{Ti}(\text{OC}_3\text{H}_7)_4$, purity (97%), density (0.96)] into a fixed 40 mL mixture volume (20 mL of methanol [(CH_3OH) , 99%] and 20 mL of acetic acid [(CH_3COOH) , 99.8%]). TTIP, methanol and acetic acid were used as precursor, solvent and catalyst, respectively. To study the effect of Ti-precursor concentration, the added volumes of TTIP were chosen to be 1, 2, 3 and 4 mL to obtain solutions with concentration of 0.084 M (aerogel S1), 0.168 M (aerogel S2), 0.252 M (aerogel S3) and 0.336 M (aerogel S4), respectively. Every solution was first magnetically stirred for about 30 min, to obtain a homogeneous mixture, and then placed in an autoclave to undergo drying in supercritical conditions of ethanol (250 °C and 70 bars).

When the supercritical conditions were reached, the solvent was rapidly removed from the autoclave which was spontaneously cooled down to room temperature. Thus, a very fine powder was recuperated and characterized without chemical or heat treatments. To study the effect

of annealing temperature, the sample S4 was annealed in air in a muffle furnace at 500 °C, 800 °C and 1000 °C for 2 h.

All the elaborated TiO_2 aerogels were analyzed by X-ray diffraction (XRD) using a PanAnalytical type diffractometer whose X-rays are produced from CuK α radiation source ($\lambda = 1.54 \text{ \AA}$) with an acceleration voltage of 40 kV and a current of 30 mA. Fourier transform infrared spectroscopy (FT-IR) analysis was carried out via a Shimadzu Irtfinity-1 type spectrometer using KBr pellet transmission (KPT) method. Scanning electron microscopy (SEM) images were taken with a Quanta Electronics 600 W type microscope. The specific surface area and pore volume were measured by the BET method using the QC Novawin 2 apparatus.

3 Results and discussion

The XRD patterns of the powder prepared with different Ti-precursor concentrations are shown in Fig. 1. All the diffraction peaks [(101), (004), (200), (105), (211), (204), (116), (220) and (215)] observed respectively at the (2θ) angles 25.20°, 37.77°, 48.03°, 54.00°, 54.84°, 62.62°, 68.82°, 70.24° and 75.12°, belong to the anatase phase of tetragonal structure which corresponds to JCPDS 00-004-0477. These results indicate that all as-prepared TiO_2 aerogels are crystallized in pure anatase phase; no traces of others phases (rutile and brookite) appeared in the patterns. It can also be seen that XRD peaks intensity increases and then decreases with Ti-precursor concentration with a maximum obtained for the aerogel S2. The relatively high peaks intensity indicates that the as-prepared aerogels are polycrystalline with good

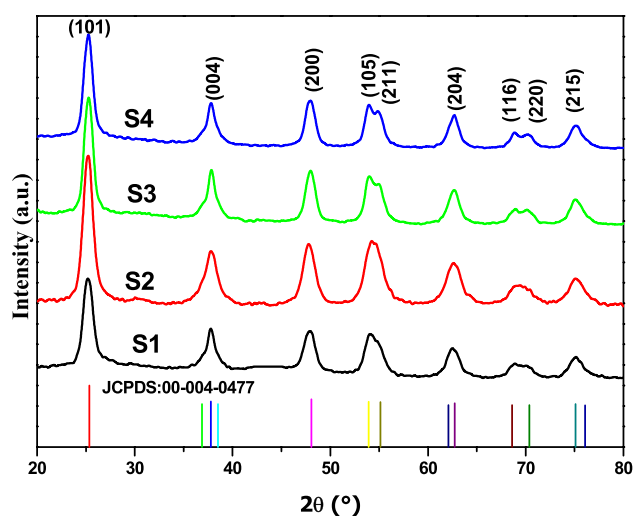


Fig. 1 XRD patterns of TiO_2 aerogels synthesized with different Ti-precursor concentrations

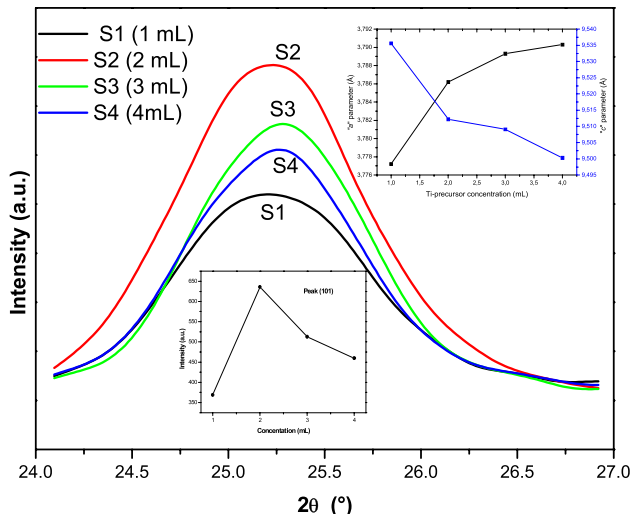


Fig. 2 (101) peak XRD patterns (in the inset, the variation of the (101) peak intensity, *a* and *c* parameters as a function of Ti-precursor concentration)

crystal quality, whereas their wide broadness indicates the nanometric scale of the crystallites.

To put into evidence the effect of the Ti-precursor concentration on the intensity of the XRD patterns, we show in Fig. 2 the (101) peak. For clarity, the inset illustrates the lattice parameters *a* and *c* and the height of the peak (101) as a function of the Ti-precursor volume. The most intense and the widest XRD patterns are obtained with 2 mL volume Ti-precursor (S2), indicating that the aerogel S2 has the best crystalline quality and the smallest crystallites. On the other hand, the opposite characteristics belong to the aerogel S1. The size of the crystallites, supposedly spherical, is calculated by Scherrer's formula:

$$D = \frac{0.89\lambda}{\beta \cos\theta} \tag{1}$$

where λ is the wavelength of the X-ray line K_{α} , θ is the diffraction angle and β is the half-height width of the diffraction peak expressed in radians. The *d*-spacing of the tetragonal crystallographic structure is given by the equation:

$$\frac{1}{d^2} = \frac{h^2 + k^2}{a^2} + \frac{l^2}{c^2}, \tag{2}$$

where *d* is distance between adjacent lattice planes and *h*, *k*, *l* are lattice vectors in Miller index notation.

The parameters of the tetragonal lattice *a* and *c* were calculated from the positions of the peaks (200) and (004), respectively, using the relations:

$$a = \frac{\lambda}{\sin\theta} \tag{3}$$

$$c = \frac{2\lambda}{\sin\theta} \tag{4}$$

The volume of the lattice is calculated from the formula:

$$V = a^2c \tag{5}$$

Table 1 regroups the crystallite size, lattice parameters, lattice volume and (101) – *d* spacing; it can clearly be seen that the smallest crystallites size is found in the aerogel S2 (7.7 nm). For the lowest concentration (aerogel S1), the cell parameters *a* and *c* are found to have minimum (3.7772 Å) and maximum (9.5356 Å) values, respectively. The smallest volume also corresponds to aerogel S1. With increasing the precursor concentration, the (101)-*d* spacing increases which indicates the expansion of the inter-planar distance in the considered direction. When the Ti-precursor concentration increases, the *a* parameter and the cell unit volume *V* increase whereas the *c* parameter decreases. These results may be explained by the chemical composition stoichiometry or by local strain exerted along *c* axis [25]. Grey et al. [26] reported that the size dependence of nanocrystalline anatase was correlated with Ti vacancy concentration in structures formed by distorted TiO₆ octaetra. Also, they demonstrated that the presence of Ti vacancies reduces the octahedral edge-sharing and relieves the strong Ti–Ti repulsion leading to obtain regular octaetra, shortened *c* parameter and lengthened *a* parameter.

In the present aerogels there are more Ti vacancies (see EDS results), the increase in *d*-spacing leads to longer O–O distances perpendicular to *c* and relatively shorter O–O distances along *c*-axis [25]. The crystallites size slightly increases with increasing Ti-precursor concentration indicating that Ti atoms are attached on the surface of the TiO₂ crystallites. This result indicates that Ti atoms, which cannot react to form the titanium oxide during the elaboration process, are located on the surface of the crystallites.

Table 1 Structural parameters of TiO₂ aerogels elaborated with different Ti-precursor concentrations

Aerogel	<i>a</i> (Å)	<i>c</i> (Å)	<i>D</i> (nm)	<i>V</i> (Å ³)	(101) – <i>d</i> – spacing (Å)
S1	3.7772	9.5356	8.3	136.04	3.511
S2	3.7862	9.5122	7.7	136.36	3.517
S3	3.7893	9.5091	8.9	136.53	3.520
S4	3.7903	9.5088	9.1	136.60	3.520

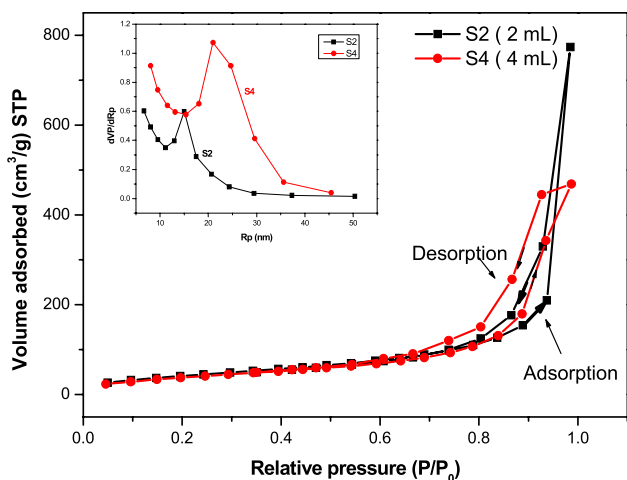


Fig. 3 N₂ adsorption–desorption isotherms for aerogels S2 and S4. In the inset BJH pore size distribution curves

In order to study the textural properties of the aerogels, nitrogen adsorption-desorption analysis at 77 K is performed. Figure 3 illustrates the Brunauer–Emmett–Teller (BET) isotherms curves of the aerogels S2 and S4. These curves show a typical type (IV) with type II like hysteresis loops, which indicates the presence of mesopores in both N–TiO₂ aerogels [27, 28]. Pore size data (BJH method) were determined using de Boer calculation method (program Quantachrome NovaWin2—Data Acquisition and Reduction for NOVA instruments). The average pore volumes are 0.510 cm³/g and 0.725 cm³/g with BET surface areas of 159.104 m²/g and 146.711 m²/g for S2 and S4, respectively. The measurements of the specific surface area by the BET method show that the average pore radius has increased substantially from 154 to 233 Å when the added volume of precursor increases from 2 to 4 mL, respectively. This certainly indicates that the increase of precursor concentration leads to an increase in total pore volume and a decrease in the density of TiO₂ aerogels. Moreover, from the isotherm curves, it can be seen that aerogel S4 possesses higher porosity than the others.

The inset of Fig. 3 shows the corresponding BJH pore size distribution curves for the titanium dioxide samples S2 and S4. Maxima at pore radii of ca. 13–16 nm and ca. 23–26 nm were observed in the mesoporous region (according to IUPAC nomenclature) for S2 and S4 samples, respectively. The changes in the pore size distributions may be due to the difference in crystallization, crystallites sizes and specific surface area as showed in Tables 1 and 2. Table 2 shows that the specific surface area of the samples decreases with increasing sol concentration, on contrary the pore size increases. Sun et al. [29] reported similar behaviors and attributed them to the crystallite growth

Table 2 Average pore diameter, total pore volume, specific surface area and crystallites size estimated by BET method

Aerogel	Average pore diameter Dp (nm)	Total pore volume Vp (cm ³ /g)	Specific area S _{BET} (m ² /g)	Crystallites size by BET method (nm)
S2	30.80	0.510	159.104	8.91
S4	46.60	0.725	146.711	9.66

mechanism and the reduction of some amorphous titania inserted into the pores of mesopores TiO₂.

Assuming that the aerogels particles have spherical shapes and same sizes, the S_{BET} can be related to the average particle size by the empirical equation [30]:

$$D_{BET} = \frac{6000}{\rho \cdot S_{BET}} \tag{6}$$

where D_{BET} is the average crystalline size (nm), ρ is the density of anatase TiO₂ (4.23 g/cm³) and S_{BET} is the BET specific surface area (m²/g). From Eq. (6) the average crystallites sizes are found to be 8.91 and 9.66 nm for the aerogels S2 and S4, respectively. These obtained results are in very good agreement consistent with XRD measurements. All the BET parameters are summarized in the Table 2.

The prepared TiO₂ anatase aerogels are also characterized by Fourier Transform Infrared Spectrometry (FTIR). The obtained spectra are shown in Fig. 4. The absorption bands characteristic of the O–H elongation located at ~ 3400 cm⁻¹ is due to the presence of some traces of water. This band is also attributed to the Ti–OH stretching modes at the TiO₂ particles surface [31]. The band located at 1630 cm⁻¹ is assigned to the Ti–OH bound vibration [31]. The peak at 2343 cm⁻¹ is attributed to the

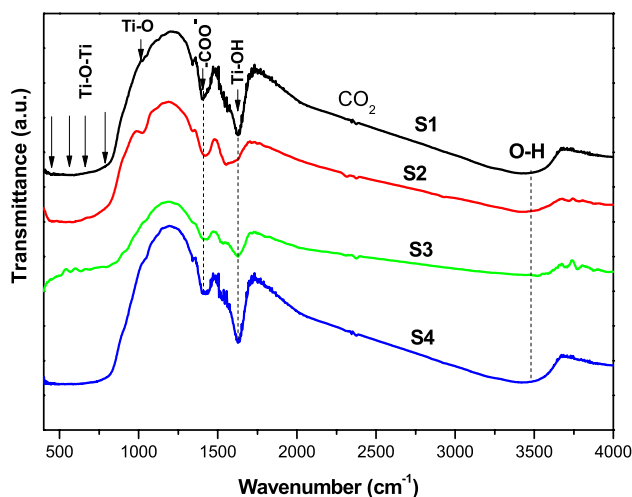


Fig. 4 FTIR spectra of TiO₂ aerogels synthesized with different Ti-precursor concentrations

asymmetric stretching of CO_2 atmospheric molecules adsorbed on the surface of the aerogels. The band at 1520 cm^{-1} could be recognized as the asymmetric stretch of COO^- [32]. The band located at 1430 cm^{-1} is assigned to the $\nu_s(\text{COO})$ symmetric stretching vibrations of the acetic acid group coordinated to Ti as a bidentate acetate ligands [33, 34]. The bands for Ti–O–Ti and Ti–O bonds are present in the $400\text{--}1100\text{ cm}^{-1}$ region, the former being observed in a very large wavenumber region [35]. This broad absorption band indicates different vibration modes of the Ti–O–Ti and Ti–O bonds which reflect the formation of TiO_2 [35, 36]. The band corresponding to the vibration of Ti–O–Ti bonds was shifted towards higher wavenumbers (1000 cm^{-1}), indicating the possible formation of Ti–O–C bonds [37].

The effect of Ti-precursor concentration on final morphology of the TiO_2 aerogels is illustrated by SEM images

in Fig. 5. The very small crystallites with quasi-spherical shape agglomerate to form grains with various morphologies and dimensions (few micrometers). The way in which the crystallites agglomerate is considerably influenced by the precursor concentration. The surfaces of the grains of samples S3 and S4 appear more smooth than those of S1 and S2. When the Ti-precursor concentration increases, the grains become smoother. We suggest that very small crystallites can easily penetrate into the large pore at the surface of the grains since the pore volume increases with Ti-precursor concentration as demonstrated by BET measurements. Thus, the outer surface of the grains appears less porous and the grains seem to have smoother surfaces.

Energy dispersion spectroscopy (EDS) patterns of anatase nano-aerogels synthesized in supercritical ethanol with different Ti-precursor concentrations are shown in Fig. 6. The results show the presence of only C, Ti and O

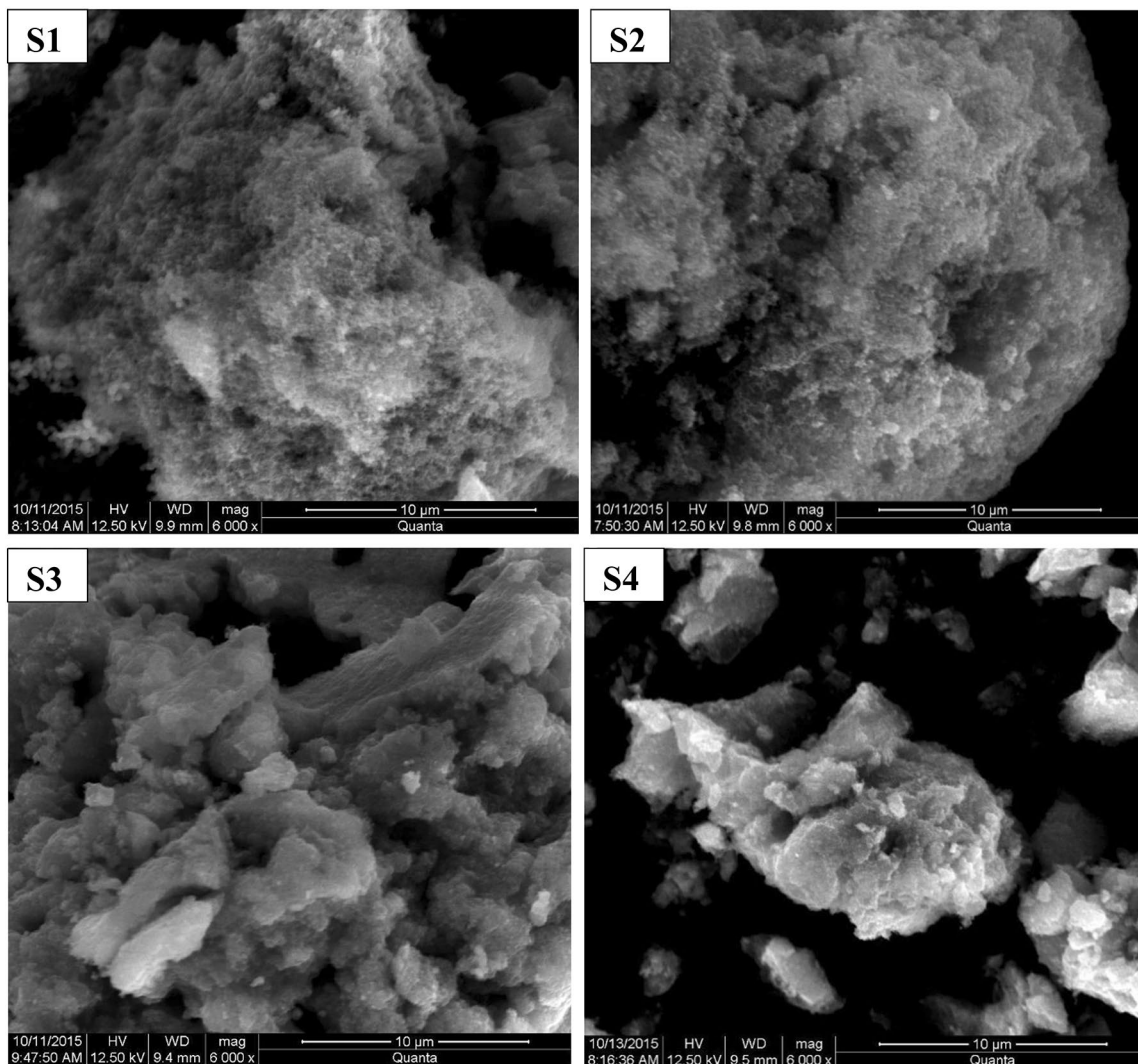


Fig. 5 SEM images of TiO_2 anatase aerogels synthesized with different Ti-precursor concentrations

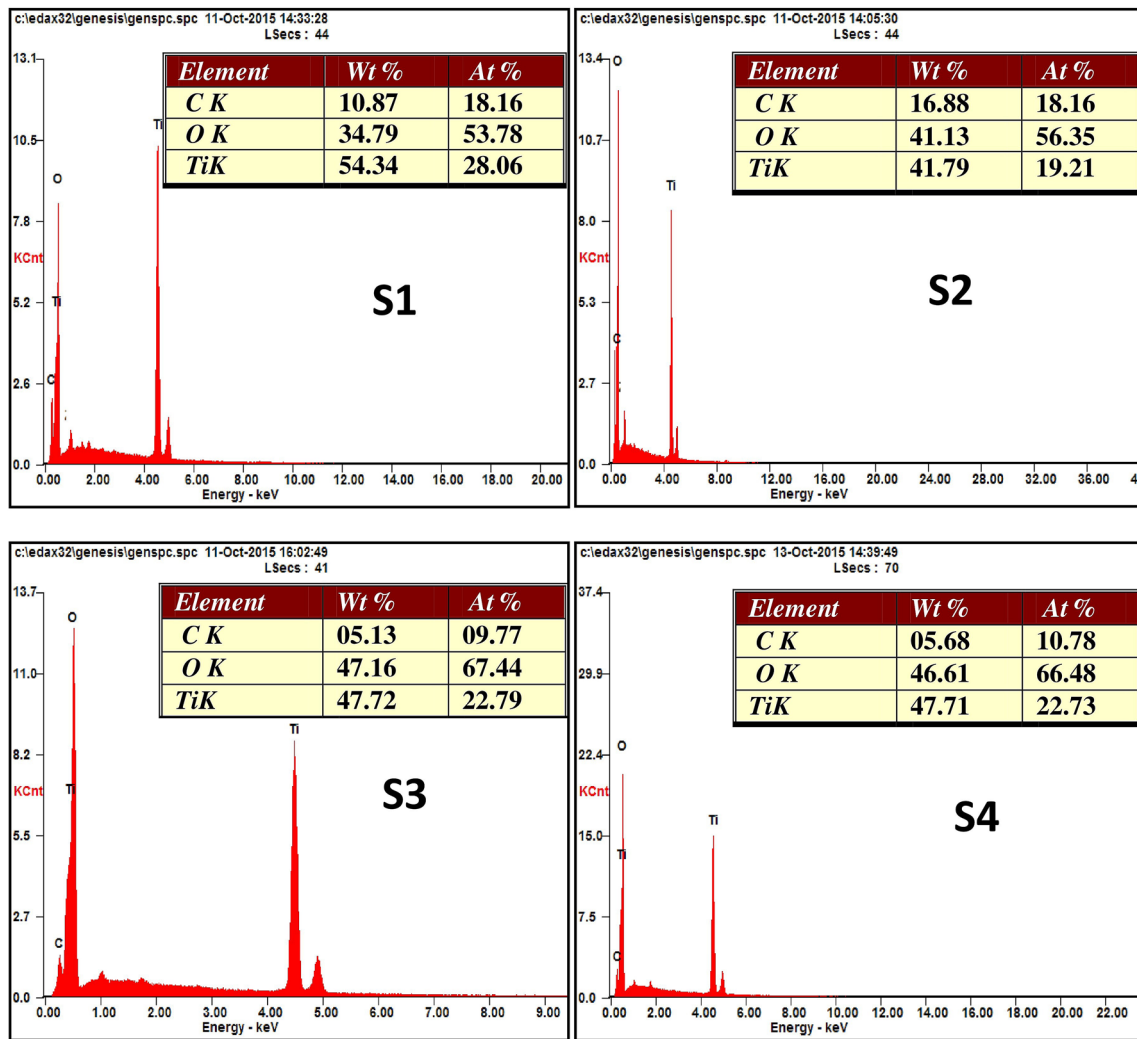


Fig. 6 EDAX results of TiO₂ aerogels synthesized with different Ti-precursor concentrations

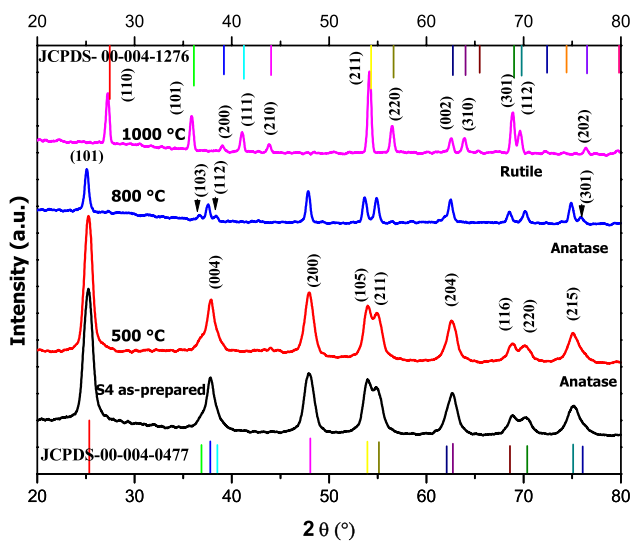


Fig. 7 XRD patterns of S4 aerogel annealed at different temperatures

atoms in the synthesized aerogels. The C atoms come probably from the grid used in the experimental set-up. All the aerogels are found to be relatively rich with oxygen atoms. The ratio [Ti]/[O] is almost the same for the samples S2, S3 and S4 (0.33), however, it is equal 0.52 for the sample S1. From these results, it seems that there is not a real relationship between Ti-precursor concentration and atomic composition of the samples. The abundance of Ti vacancies leads to a reduction in the number of TiO₆ octahedra in the structure, and consequently, a decrease in *c* parameter and an increase in *a* parameter as confirmed by XRD measurements.

To investigate the effects of annealing temperature on structural and morphological properties of TiO₂ aerogels and to determine the anatase–rutile transition temperature, the S4 aerogel was annealed at 500, 800 and 1000 °C in air for 2 h. Figure 7 represents the XRD patterns of this aerogel annealed at different temperatures. The intensity

of the peaks slightly increases with annealing at 500 °C and decreases for the aerogel annealed at 800 °C. This behavior indicates that the initial annealing process at 500 °C improves the crystalline quality of the as-prepared aerogel whereas subsequent annealing temperatures lead to the inverse effect.

Up to 800 °C, the aerogels are crystallized in pure polycrystalline anatase phase. With increasing of annealing temperature, the intensity of the peaks decreases, indicating the gradual disappearance of the anatase phase (without rutile phase emergence). The decrease in the XRD peaks intensity might be due to the transformation of anatase phase to rutile. At 1000 °C, the pure anatase phase is completely transformed to pure rutile phase without simultaneous phases coexistence. In this case, the anatase–rutile transition temperature is found to be between 800 and 1000 °C; in this temperatures range, the anatase phase is completely transformed to rutile. It is worth noting that the temperature of anatase to rutile transformation is generally dependent on various experimental parameters, synthesis method, chemical composition and additional impurities into TiO₂ crystals [38–40]. Generally, anatase and rutile phases exist simultaneously (anatase–rutile TiO₂ mixture) in a large range of temperatures. For example, the metastable anatase is completely transformed to stable rutile phase at 600 °C [41], at 700 °C [42] and at 900 °C [43]. Thermodynamic studies demonstrated that metastable anatase transforms irreversibly to stable rutile at high temperature with different transition temperatures and involved processes. This is due to the fact that TiO₂ phases generation depends on all the synthesis conditions (particle size and shape, impurities, heating rate, measurements conditions, etc.). Anatase–rutile transformation is a nucleation and growth process. In pure anatase, it has been reported that rutile nucleates at (112) interface in anatase as these sites are structurally similar to rutile [40]. Rutile is reported to exhibit oxygen deficiency and the oxygen vacancies in anatase can be expected to enhance the transformation to rutile owing to the facilitated rearrangement of ions [44]. In the present work, the annealing in air of anatase leads to increase the number of oxygen vacancies in the anatase lattice by promoting the transformation to rutile and the transition temperature occurs between 800 and 1000 °C.

Table 3 Structural parameters of S4 aerogel annealed at different temperatures

Sample	Phase nature	a (Å)	c (Å)	D (nm)	V (Å ³)
As-prepared (S4)	Pure anatase	3.7954	9.5088	8.76	136.97
500 °C (S4)	Pure anatase	3.7891	9.5003	9.74	136.39
800 °C (S4)	Pure anatase	3.7965	9.5654	18.32	137.87
1000 °C (S4)	Pure rutile	4.6100	2.9659	16.6	63.03

For the annealed aerogel at 1000 °C, all the diffraction peaks [(110), (101), (200), (111), (210), (211), (220), (002), (310), (301) and (112)] observed at the (2θ) angles 27.24°, 35.86°, 39.03°, 41.04°, 43.81°, 54.14°, 56.51°, 62.56°, 63.93°, 68.90° and 69.63°, respectively, belong to the rutile phase of tetragonal structure which corresponds to JCPDS 00-004-1276. The lattice parameters *a* and *c* of the anatase and rutile phases, crystallites size and the unit cell volume are calculated and shown in Table 3.

These results indicate that there is an increase in crystallite size from the as-prepared aerogel to the aerogel annealed at 800 °C. Moreover, it should be noted that cell parameters (*a* and *c*) and the unit cell volume *V* of pure anatase phase decrease when annealing temperature increases from room temperature to 500 °C and then increase until the anatase–rutile transition temperature. The lattice parameters of the tetragonal polycrystalline rutile phase are *a* = *b* = 4.6100 Å and *c* = 2.9659 Å with a unit cell volume equal to 63.03 Å³. The crystallites size also increases with increasing annealing temperature. This increase may be due to the fact that the crystallite growths can be related to the removal of oxygen ions migration towards the outer side of the particles [45]. It is well known that anatase is a metastable phase and its conversion to rutile involves an irreversible collapse of the anatase structure. The collapse from anatase to higher density rutile presupposes the transformation of an elongated side-to-side packing (anatase) to a close packed arrangement (rutile). This transformation can be enhanced or impeded by influencing the rearrangement of the atoms in the anatase and rutile lattices [40].

FTIR spectra of S4 aerogel annealed at different temperatures are shown in Fig. 8. With increasing annealing

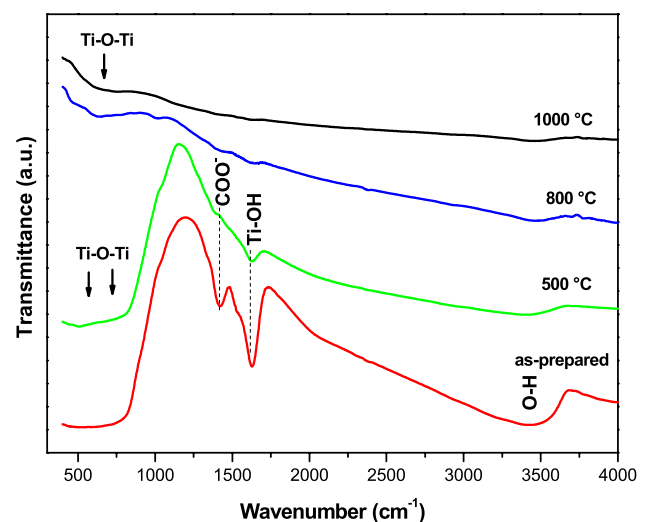


Fig. 8 FTIR spectra of S4 aerogel annealed at different temperatures

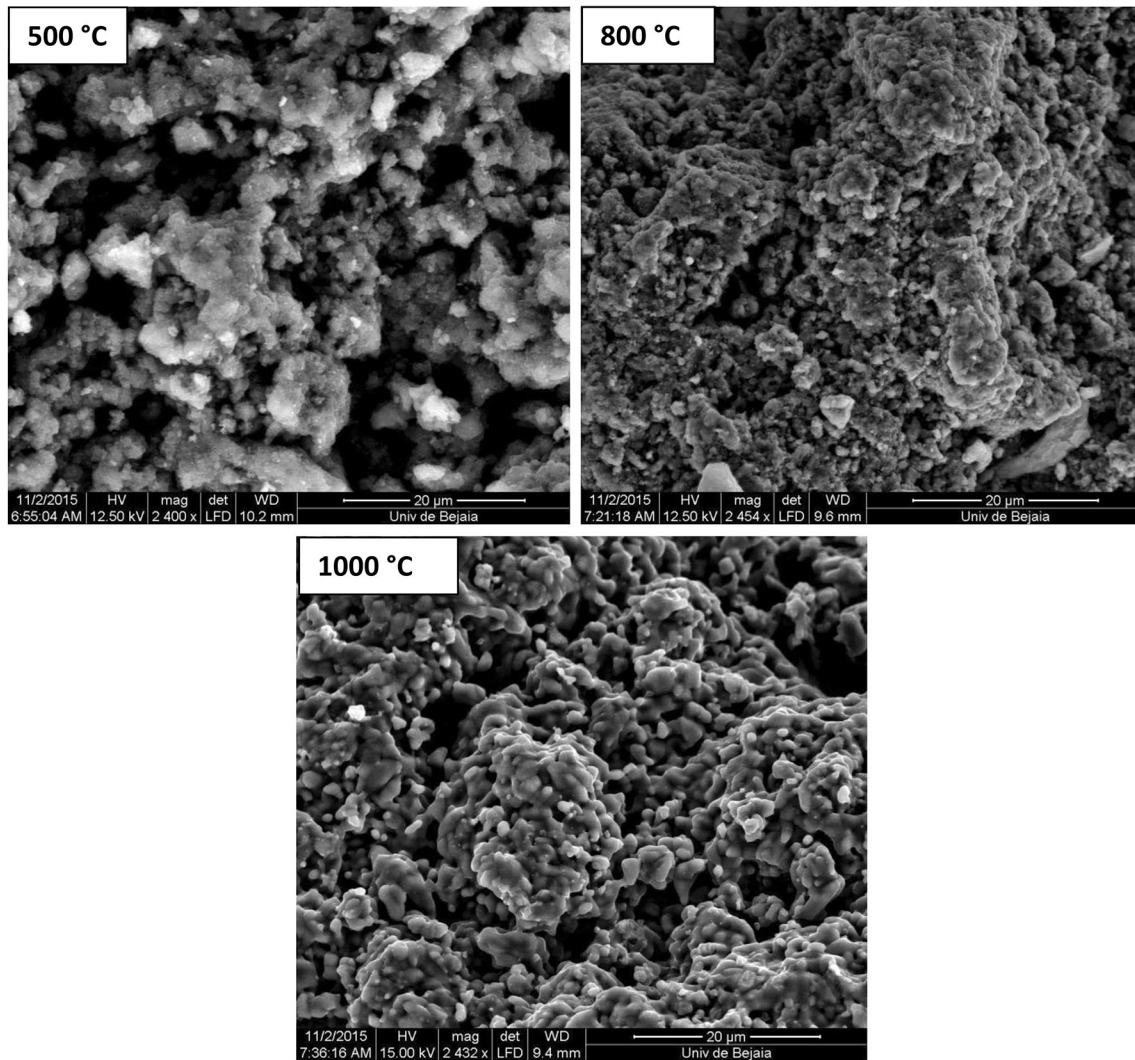


Fig. 9 SEM images of S4 aerogel annealed at different temperatures

temperature, the intensity of the absorption bands assigned to COO^- , Ti-OH and O-H vibration bonds decreases and these bands disappear completely at $800\text{ }^\circ\text{C}$. Ti-O-Ti absorption band shifts towards low wavenumbers side with increasing the annealing temperature. The decrease of these bands intensity might be due to the structural phase transformation [46]. The shifting of the absorption band corresponding to Ti-O stretching to lower wavenumbers side with increasing the annealing temperature indicates a decrease in the strength of Ti-O bond and the elimination of Ti-O-C bonds due to thermal treatment.

Figure 9 shows SEM images of S4 aerogel annealed at 500, 800 and $1000\text{ }^\circ\text{C}$. As can be seen, the grains of the

as-prepared aerogel (Fig. 5) are more dispersed and give a less dense appearance. On the other hand, the texture of the annealed aerogels (Fig. 9), resulting from the agglomeration of roughly spherical particles, looks slightly compact and smooth. This can be explained by the evacuation by the air molecules and the elimination of organic compounds with heat treatment. The purity of TiO_2 crystallites chemically enhanced and annealing greatly favors the agglomeration process to form relatively smooth and large grains. The SEM image of the S4 aerogel annealed at $1000\text{ }^\circ\text{C}$ (rutile phase) indicates that the annealing process not only changes the crystalline structure of the particles but also the morphology of the grains.

4 Conclusion

In this work, titania nano-aerogels have been prepared by sol-gel method associated with drying in supercritical conditions of ethanol. The effects of precursor concentration and annealing temperature on structural and morphological properties of TiO₂ aerogels have been investigated. The XRD analysis has revealed that pure anatase phase is obtained for the aerogels synthesized with various precursor concentrations with crystallite size less than 10 nm. The unit cell parameters vary uniformly with Ti-precursor concentration. The highest specific surface area was found in S2 aerogel. The pore volume increases with increasing sol concentration. The presence of Ti–O and Ti–O–Ti bonds was confirmed by FTIR measurements. EDAX analysis has indicated that the elaborated powders are oxygen rich whereas, SEM images have shown that the nanoparticles are nearly spherical with larger agglomeration at high precursor concentration. The annealing temperature study did not show the emergence of phase's mixture. The anatase–rutile phase transition temperature was found to be around 900 °C. Finally, it was found that the increase in annealing temperature leads to a shift of Ti–O–Ti absorption band towards lower wave numbers side due to the Ti–O–C bonds rupture.

Compliance with ethical standards

Conflict of interest On behalf of all authors, the corresponding author states that there is no conflict of interest.

References

1. Castillo N, Olguin D, Conde-Gallardo A, Jiménez-Sandoval S (2004) Structural and morphological properties of TiO₂ thin films prepared by spray pyrolysis. *Rev Mex Física* 50(4):382–387
2. Kubacka A, Fernandez-Garcia M, Colon G (2011) Advanced nano-architectures for solar photocatalytic applications. *Chem Rev* 112(3):1555–1614
3. Abbad S, Guergouri K, Gazaout S, Djebabra S, Zertal A, Barille R, Zaabat M (2020) Effect of silver doping on the photocatalytic activity of TiO₂ nanopowders synthesized by the sol-gel route. *J Environ Chem Eng* 8:103718–103727
4. Wang J, Tafen DN, Lewis JP, Hong Z, Manivannan A, Zhi M, Li M, Wu N (2009) Origin of photocatalytic activity of nitrogen-doped TiO₂ nanobelts. *J Am Chem Soc* 131(34):12290–12297
5. Sun L, Zhao X, Cheng X, Sun H, Li Y, Li P, Fan W (2012) Synergistic effects in La/N codoped TiO₂ anatase (101) surface correlated with enhanced visible-light photocatalytic activity. *Langmuir* 28(13):5882–5891
6. Romero Saez M, Jaramillo L, Saravanan R, Benito N, Pabón E, Mosquera E, Gracia Caroca F (2017) Notable photocatalytic activity of TiO₂-polyethylene nanocomposites for visible light degradation of organic pollutants. *Express Polym Lett* 11:899–909
7. Kang X, Liu S, Dai Z, He Y, Song X, Tan Z (2019) Titanium dioxide: from engineering to applications. *Catalysts* 9(2):191
8. Feng Y, Li L, Ge M, Guo C, Wang J, Liu L (2010) Improved catalytic capability of mesoporous TiO₂ microspheres and photodecomposition of toluene. *ACS Appl Mater Interfaces* 2(11):3134–3140
9. Chen X, Sun H, Zhang J, Zelekew OA, Lu D, Kuo D-H, Lin J (2019) Synthesis of visible light responsive iodine-doped mesoporous TiO₂ by using biological renewable lignin as template for degradation of toxic organic pollutants. *Appl Catal B* 252:152–163
10. Zhang C, Liu F, Zhai Y, Ariga H, Yi N, Liu Y, Asakura K, Flytzani-Stephanopoulos M, He H (2012) Alkali-metal-promoted Pt/TiO₂ opens a more efficient pathway to formaldehyde oxidation at ambient temperatures. *Angew Chem Int Ed* 51(38):9628–9632
11. Bavykin DV, Friedrich JM, Walsh FC (2006) Protonated titanates and TiO₂ nanostructured materials: synthesis, properties, and applications. *Adv Mater* 18(21):2807–2824
12. Singh DP, Ali N (2010) Synthesis of TiO₂ and CuO nanotubes and nanowires. *Sci Adv Mater* 2(3):295–335
13. Bickley RI, Gonzalez-Carreno T, Lees JS, Palmisano L, Tilley RJ (1991) A structural investigation of titanium dioxide photocatalysts. *J Solid State Chem* 92(1):178–190
14. Zhang Q, Gao L, Guo J (2000) Effects of calcination on the photocatalytic properties of nanosized TiO₂ powders prepared by TiCl₄ hydrolysis. *Appl Catal B* 26(3):207–215
15. Tanaka K, Capule MF, Hisanaga T (1991) Effect of crystallinity of TiO₂ on its photocatalytic action. *Chem Phys Lett* 187(1–2):73–76
16. Ohtani B, Zhang S-W, Handa J, Kajiwara H, Nishimoto S, Kagiya T (1992) Photocatalytic activity of titanium(IV) oxide prepared from titanium(IV) tetra-2-propoxide: reaction in aqueous silver salt solutions. *J Photochem Photobiol A* 64(2):223–230
17. Lai C, Zhou X, Huang D, Zeng G, Cheng M, Qin L, Yi H, Zhang C, Xu P, Zhou C (2018) A review of titanium dioxide and its highlighted application in molecular imprinting technology in environment. *J Taiwan Inst Chem Eng* 91:517–531
18. Carbajo J, Tolosana-Moranchel A, Casas J, Faraldos M, Bahamonde A (2018) Analysis of photoefficiency in TiO₂ aqueous suspensions: effect of titania hydrodynamic particle size and catalyst loading on their optical properties. *Appl Catal B* 221:1–8
19. Momeni MM, Hakimian M, Kazempour A (2015) In-situ manganese doping of TiO₂ nanostructures via single-step electrochemical anodizing of titanium in an electrolyte containing potassium permanganate: a good visible-light photocatalyst. *Ceram Int* 41(10):13692–13701
20. Savio A, Fletcher J, Smith K, Iyer R, Bao J, Hernández FR (2016) Environmentally effective photocatalyst CoO–TiO₂ synthesized by thermal precipitation of Co in amorphous TiO₂. *Appl Catal B* 182:449–455
21. Reinke M, Ponomarev E, Kuzminykh Y, Hoffmann P (2015) Combinatorial characterization of TiO₂ chemical vapor deposition utilizing titanium isopropoxide. *ACS Combin Sci* 17(7):413–420
22. Yue X, Xiang J, Chen J, Li H, Qiu Y, Yu X (2020) High surface area, high catalytic activity titanium dioxide aerogels prepared by solvothermal crystallization. *J Mater Sci Technol* 47:223–230
23. Stucchi M, Bianchi C, Argiris C, Pifferi V, Neppolian B, Cerrato G, Boffito D (2018) Ultrasound assisted synthesis of Ag-decorated TiO₂ active in visible light. *Ultrason Sonochem* 40:282–288
24. Vetrivel V, Rajendran K, Kalaiselvi V (2015) Synthesis and characterization of pure titanium dioxide nanoparticles by sol-gel method. *Int J Chem Technol Res* 7:1090–1097
25. Kuznetsov AY, Machado R, Gomes LS, Achete CA, Swamy V, Muddle BC, Prakapenka V (2009) Size dependence of rutile TiO₂ lattice parameters determined via simultaneous size, strain, and shape modeling. *Appl Phys Lett* 94(19):193117–193123

26. Grey IE, Wilson NC (2007) Titanium vacancy defects in sol–gel prepared anatase. *J Solid State Chem* 180(2):670–678
27. Donohue MD, Aranovich G (1999) A new classification of isotherms for Gibbs adsorption of gases on solids. *Fluid Phase Equilib* 158:557–563
28. Bagwasi S, Tian B, Zhang J, Nasir M (2013) Synthesis, characterization and application of bismuth and boron Co-doped TiO₂: a visible light active photocatalyst. *Chem Eng J* 217:108–118
29. Su Y, Yu J, Lin J (2007) Vapor-thermal preparation of highly crystallized TiO₂ powder and its photocatalytic activity. *J Solid State Chem* 180(7):2080–2087
30. Raoufi D (2013) Synthesis and microstructural properties of ZnO nanoparticles prepared by precipitation method. *Renew Energy* 50:932–937
31. Lopez T, Gomez R, Sanchez E, Tzompantzi F, Vera L (2001) Photocatalytic activity in the 2,4-dinitroaniline decomposition over TiO₂ sol-gel derived catalysts. *J Sol-Gel Sci Technol* 22(1–2):99–107
32. Li H, Liu B, Yin S, Sato T, Wang Y (2015) Visible light-driven photocatalytic activity of oleic acid-coated TiO₂ nanoparticles synthesized from absolute ethanol solution. *Nanoscale Res Lett* 10(1):415
33. Vasconcelos DCL, Costa VC, Nunes EHM, Sabioni ACS, Gasparon M, Vasconcelos WL (2011) Infrared spectroscopy of titania sol-gel coatings on 316L stainless steel. *Mater Sci Appl* 2(10):1375–1382
34. Moussaoui R, Elghniji K, de Mosbah M, Elaloui E, Moussaoui Y (2017) Sol–gel synthesis of highly TiO₂ aerogel photocatalyst via high temperature supercritical drying. *J Saudi Chem Soc* 21(6):751–760
35. Djaoued Y, Badilescu S, Ashrit P, Robicahud J (2001) Vibrational properties of the sol–gel prepared nanocrystalline TiO₂ thin films. *The Internet J Vibr Spectrosc* 5:6
36. Ghamsari MS, Bahramian A (2008) High transparent sol-gel derived nanostructured TiO₂ thin film. *Mater Lett* 62(3):361–364
37. Zhang H, Lv X, Li Y, Wang Y, Li J (2009) P25-graphene composite as a high performance photocatalyst. *ACS Nano* 4(1):380–386
38. Ogacho AA, Ajuoga P, Aduda B (2015) Suppression of anatase to rutile phase transformation of niobium doped TiO₂ synthesized by high temperature diffusion technique. *Int J Innov Educ Res*. <https://doi.org/10.31686/ijer.vol3.iss6.388>
39. Castrejón-Sánchez V, López R, Ramón-González M, Enríquez-Pérez Á, Camacho-López M, Villa-Sánchez G (2019) Annealing control on the anatase/rutile ratio of nanostructured titanium dioxide obtained by sol–gel. *Crystals* 9(1):22
40. Hanaor DA, Sorrell CC (2011) Review of the anatase to rutile phase transformation. *J Mater Sci* 46(4):855–874
41. Wetchakun N, Incessungvorn B, Wetchakun K, Phanichphant S (2012) Influence of calcination temperature on anatase to rutile phase transformation in TiO₂ nanoparticles synthesized by the modified sol–gel method. *Mater Lett* 82:195–198
42. Arbiol J, Cerda J, Dezanneau G, Cirera A, Peiro F, Cornet A, Morante J (2002) Effects of Nb doping on the TiO₂ anatase-to-rutile phase transition. *J Appl Phys* 92(2):853–861
43. Kumar K-NP, Fray DJ, Nair J, Mizukami F, Okubo T (2007) Enhanced anatase-to-rutile phase transformation without exaggerated particle growth in nanostructured titania–tin oxide composites. *Scr Mater* 57(8):771–774
44. Dang Y, West AR (2019) Oxygen stoichiometry, chemical expansion or contraction, and electrical properties of rutile, TiO₂±δ ceramics. *J Am Ceram Soc* 102(1):251–259
45. Singh PK, Mukherjee S, Ghosh CK, Maitra S (2017) Spectroscopic investigation on sol gel derived TiO₂ nanoparticles. *J Adv Nanomater* 2(3):161
46. Singh MK, Mehata MS (2019) Phase-dependent optical and photocatalytic performance of synthesized titanium dioxide (TiO₂) nanoparticles. *Optik* 193:163011–163111

Publisher's Note Springer Nature remains neutral with regard to jurisdictional claims in published maps and institutional affiliations.